The effect of edge compliance on the adhesive contact between a spherical indenter and a quarter-space

Gheorghe Stan

Material Measurement Laboratory, National Institute of Standards and Technology, Gaithersburg, Maryland, USA

E-mail: gheorghe.stan@nist.gov

Abstract

In this work, the effect of the edge compliance on the adhesive, frictionless contacts near the edge of a quarter-space is analyzed in terms of stress, deformation, and contact stiffness. The study relies on the numerical implementation of the conjugate gradient method (CGM) to adhesive contacts near the edge of a quarter-space. It extends the previous CGM developed for contact analysis of non-adhesive and adhesive contacts on half-space to the matrix formulation of the quarter-space problem. The considered adhesive contact interaction is in terms of the Maugis-Dugdale model to provide insight into the transitional behavior from non-adhesive to various type of contact adhesive regimes. It is found that the edge compliance affects the contact mechanics of adhesive contacts as a function of position, applied force, and adhesive parameter. The analysis provides calculations for quantities like depth indentation and contact stiffness that can be found directly in indentation-type experiments performed on samples with edge geometries. Such understanding and characterization of edge contacts can be used to unambiguously account for the mechanical response of nanoscale structures near their edges and detect possible mechanical variability introduced by fabrication and processing.

Keywords: edge compliance, indentation, contact stiffness

1. Introduction

The ability to properly account for the edge effect on the contact mechanics of a quarter-space subjected to loads nearby its edge is relevant to various types of applications from macroscale (rolling-element bearings, rail wheels, gears, etc.) (Hanson and Keer, 1991; Yu and Keer, 1996) to microscale (micro- and nano- electromechanical systems, mechanical testing of micro- and nano-scale specimens, etc.) (Jakes et al., 2009; Jakes and Stone, 2010). It can be used to correctly solve the stress field around loaded edges and identify possible mechanical heterogeneities at the edge of fabricated specimens. Although the problem of an elastic half-space (HS) subjected to concentrated loads is well known and commonly used to interpret measurements, less investigated and almost unused in data analysis is its counterpart quarter-space (QS) configuration. One impediment to dealing with the QS problem is the lack of an analytical solution. On the other hand, numerical calculations like finite element method and boundary element method are time consuming and strenuous for analysis of contact mechanics measurements on QS specimens. However, with the increase in computational power, various numerical calculation methods for QS mechanics will become more affordable and practical for interpreting mechanical property measurements on micro- and nano-scale specimens with protruding topographical features (*e.g*. atomic force microscopy measurements on nanoscale high-aspect ratio geometries) (Stan et al, 2016; Stan et al., 2017).

The QS problem was introduced by Hetenyi about 50 years ago (Hetenyi, 1970) as a reflection iterative method of two overlapped half-spaces to examine the elastic response of a QS under the action of a normal concentrated load. The resulting integral equations were solved numerically by using Love's patch solution (Love, 1929) on discretized surfaces. Keer et al. (Keer et al., 1983) reformulated the Hetenyi's analysis for a concentrated load on a QS in terms of Fourier transform to reduce the QS problem to two decouple integral equations in a quarter-plane and solved them by the Gauss-Legendre integration method. Subsequently, this method was simplified by Hanson and Keer (Hanson and Keer, 1990) to directly solve the two integral equations for each element of the meshes used to discretize the involved HS surfaces. Solution

for an arbitrary prescribed load on an elastic QS was provided by Keer et al. (Keer et al., 1984) based on a discretization method introduced by Armani et al. (Armani et al., 1983) for non-Hertzian contacts on a HS, with example of a rigid frictionless cylinder indenting an elastic QS. Recently, the QS problem was explicitly solved by Zhang et al. (Zhang et al., 2013) in a matrix formulation with direct solution for the Hetenyi's infinite iteration. The matrix formulation was also extended to rectangular fin geometries that include two free-end surfaces (Zhang et al., 2016).

An important physical property unaccounted in the above QS contact mechanics examinations is the adhesive interaction between the indenter and the QS probed. The adhesion becomes relevant especially at small scale and loads comparable with the adhesive forces. In the absence of adhesion, the contact mechanics between two homogeneous, elastically deformable, solids is commonly described by the Hertz model (Hertz, 1881; Huber, 1904; Johnson, 1985; Hills et al., 1993). The assumptions of the Hertz model are that the two solids have continuous and non-conforming surfaces, the induced strains are small, the solids can be considered as elastic half-spaces, and the surfaces are frictionless and non-adhesive (Johnson, 1985). However, the contact mechanics complicates when the adhesive contact interaction needs to be considered. Over the years, various models were proposed to describe the adhesive contact between two elastically deformable solids, most notably being the Derjaguin-Muller-Toporov (DMT) model (Derjaguin et al., 1975) that considers that the adhesive forces act only outside the contact area and Johnson-Kendall-Roberts (JKR) model (Johnson et al., 1971) that assumes that the adhesive forces occur only inside contact area. The DMT limit is valid in the case of stiff materials with low surface energy and small radius of curvature and the JKR limit works for compliant materials with large surface energy and large radius of curvature. A continuous transition between DMT and JKR extremes is achieved by the Maugis-Dugdale (MD) model (Maugis, 1992) that assumes the existence of a uniform tensile stress σ_0 within an annular region $a < r < c$ outside the contact zone where the separation between the indenter and the HS surface is less than $h_0 = w/\sigma_0$. Here a is the contact radius, c is the adhesion radius, and w is the work of adhesion. The MD model solved few theoretical caveats of the DMT and JKR models (*e.g.* the adhesive force cannot deform the surface in the DMT model; stress singularity at the contact edge in the JKR model) by

providing a continuous transition in the tensile stress at the edge of the contact. The Maugis parameter that assures this transition is defined as

$$\lambda = 2\sigma_0 \left(\frac{R}{\pi w K^2}\right)^{1/3}, \tag{6}$$

with $K = 4E/(3(1-\nu^2))$, E and ν the Young's modulus and Poisson's ratio of the indented sample (the indenter is considered here infinitely rigid), and R the equivalent radius of curvature of the two bodies in contact, which for the HS geometry reduces to the radius of the indenter. The MD model reaches the DMT limit when λ approaches zero and recovers the JKR limit for infinite λ (in practice large values of λ provide good approximation for the JKR limit).

It is the purpose of this work to examine how the adhesive contacts nearby the edge of a QS are affected by the presence of the free-edge of the QS. In the absence of closed analytical models for such geometries, the analysis is performed here by using a boundary finite method (BEM) with calculations for the stress and deformation fields around the contacts points and the load dependence of the contact stiffness, a quantity that is commonly measured in contact mechanical tests. Also, of theoretical and practical relevance is the observation of these parameters as a function of distance from the free edge of the QS to provide a clear evaluation of the edge effect. The adhesion is considered as in the MD model to account for various type of adhesive interactions encountered in contact mechanics.

The current application of the BEM to MD adhesive contacts on QS follows the numerical implementation of the conjugate gradient method used by Bazrafshan et al. (Bazrafshan et al., 2017) and Rey et al. (Rey et al., 2017) to analyze adhesive normal contacts on a HS. The extension to the QS case is made through the matrix formulation of Zhang et al. (Zhang et al., 2013) for non-adhesive contact mechanics on QS. Baseline comparisons for the BEM analysis developed in this work are provided with respect to few non-adhesive and adhesive HS contact examples (Johnson, 1985; Maugis, 1992) of known analytical solution. For the QS case, the comparison is only with respect to non-adhesive QS contact geometries of prescribed contact stress that were solved previously (Hanson and Keer, 1990; Zhang et al., 2013). As the adhesive QS contacts were not investigated yet, the current work provides results for such geometries, with numeric analysis

for the force dependence of the indentation depth and contact stiffness as a function of contact position from the edge of the QS.

2. Boundary element method for Hertz and Maugis-Dugdale contact mechanics on a half-space

In the BEM applied to the contact between two solids, the deformation-stress integrals are numerically solved over the loaded surface while satisfying the given boundary conditions. For the case of a rigid indenter loaded on a HS, the discretization is made only on a target region of the HS where stresses and deformation are prominent, usually of the order of few contact radii. As shown in Figure 1a, each surface of the calculation region was discretized in a finite number of N^2 rectangular cells, with N grid points and $2\Delta s$ grid spacing on each axis. In this mesh representation, the load distribution on the *XY*-plane (H-surface) is approximated by a piecewise distribution, with uniform load over each cell. For the HS problem only the H-surface of the space is considered whereas for the QS problem both the H-surface and V-surface will be included.

When the indenter is brought into contact with the HS under a given load F, neither the distribution of the contact pressure distribution over the contact area nor the actual contact area are known. They need to be solved at each nod of the grid together with the established contact geometry to determine the contact pressure distributed by the applied load over the contact. Quite generally, the contact pressure distribution p over the indented H-surface is defined with respect to the contact geometry, namely the indenter-surface separation g, as:

$$\begin{cases} p_{ij} < 0 \text{ at } g_{ij} = 0 \\ p_{ij} = 0 \text{ at } g_{ij} > 0 \end{cases}, \quad \text{with } i,j \in \{1,2,\dots,N\} \tag{10}$$

for the Hertz contact and

$$\begin{cases} p_{ij} < \sigma_0 \text{ at } g_{ij} = 0 \\ p_{ij} = \sigma_0 \text{ at } 0 < g_{ij} < h_0, \\ p_{ij} = 0 \text{ at } g_{ij} > h_0 \end{cases} \quad \text{with } i,j \in \{1,2,\dots,N\} \tag{11}$$

for a MD contact, such that the applied load sums up to

$$F = -4\Delta s\Delta s \sum_{i=1}^{N}\sum_{j=1}^{N} p_{ij} \tag{12}$$

in each case. The convention here is to have negative values for compressive stresses and positive for tensile stresses (Maugis, 1992).

For the considered spherical indenter of radius R, the separation between the indenter and the H-surface over the defined mesh is given by

$$g_{ij} = \frac{1}{2R}\left[(x_i - x_c)^2 + y_j^2\right] - \delta + u_z^{ij}, \text{ with } i,j \in \{1,2,\dots,N\} \tag{13}$$

where δ is the relative rigid approach of the two surfaces (also referred to as indentation depth) and u_z^{ij} is the surface deformation at position (x_i, y_j).

Once the contact pressure distribution p over the H-surface is assigned (Equation 10 or 11), the components of the generated stress and deformation fields at a given nod (k,l) of the grid can be calculated by summing up the contributions from all the loaded patches of the H-surface:

$$\sigma_{qr}^{kl} = \sum_{i=1}^{N}\sum_{j=1}^{N} \mathbf{S}_{qr}^{k-i,l-j}\, p_{ij}, \text{ with } k,l \in \{1,2,\dots,N\} \tag{14}$$

and

$$u_q^{kl} = \sum_{i=1}^{N}\sum_{j=1}^{N} \mathbf{U}_{q}^{k-i,l-j}\, p_{ij}, \text{ with } k,l \in \{1,2,\dots,N\} \tag{15}$$

with the influence matrix coefficients $\mathbf{S}$ and $\mathbf{U}$ given by the Love's solution for a uniformly loaded rectangular patch (Love, 1929). The subindices q and r are for the components x, y, and z of stresses and deformations. A review of the Love's rectangular patch solution for computational contact analyses based on FFT algorithms can be found in Jin et al. (Jin et al., 2016).

It is noted that the above expressions are in the form of convoluted functions that can be easily converted in direct products in the Fourier space. So rather than applying the conventional direct multiplication method, these convolutions can be processed by the discrete convolution and fast Fourier transform (DC-FFT) algorithm introduced by Liu et al. (Liu et al., 2000) Through this DC-FFT algorithm a linear discrete convolution is embedded into a circular discrete

convolution of double length. To do that, the calculation domain (H-surface) will be doubled on each dimension with zero-padding on the contact pressure matrix and wrap-around order (mirror) of the influence coefficient matrix over the added area. The benefit of performing the discrete circular convolution is that the circulant matrix of the influence coefficients contains only one column of independent elements (each row of a circulant matrix is obtained by one-step shift of the previous ones) and the response is obtained as the inverse FFT of the direct product of the FFTs of the influence coefficient and contact pressure distribution matrices (similarly to a linear convolution in the continuous space):

$$\bar{\bar{u}}_{ij} = \mathrm{IFFT}\left(\mathrm{FFT}\left(\bar{\bar{\mathbf{U}}}\right)_{ij} \cdot \mathrm{FFT}(\bar{p})_{ij}\right), \quad \text{with } i,j \in \{1,2,\dots,N,N+1,\dots,2N\} \tag{16}$$

where $\bar{\bar{\mathbf{U}}}$ is the wrap-around order of $\mathbf{U}$ and $\bar{p}$ is the zero-padding of p. The actual deformation matrix u is collected from the first $N \times N$ elements of $\bar{\bar{u}}$,

$$u_{ij} = \bar{\bar{u}}_{ij}, \quad \text{with } i,j \in \{1,2,\dots,N\}. \tag{17}$$

The non-linear contact problem defined above by Equations 10 to 13 can be seen as an optimization problem with inequality constrains (also known as Kuhn-Tucker conditions). Thus, the contact pressure distribution can be solved over the defined grid by minimizing the surface gap g between the indenter and the indented surface through an optimization algorithm like the conjugate gradient method (CGM, Shewchuk, 1994). The CGM is used to solve numerically a positive definite system of linear equations by iteratively searching to minimize a quadratic function whose gradient matches the system of equations. The search for the zero solution of the function's gradient is performed in CGM along conjugate directions (conjugate with respect to the coefficient matrix of the system of equations) in contrast to the more intuitive steepest descent method where the search is pursued along gradient directions. Because the conjugate directions are linearly independent of each other, the CGM does not repeat any previous search direction as the steepest descent does, hence the CGM is computational efficient in converging towards the final solution in a finite number of steps (less or equal with the number of equations). At each iteration step of the CGM there is a direct convergence in contrast to the zig-zag path followed by the steepest descent method. Also, not all the conjugate directions are needed to be

calculated at the beginning of the algorithm but they are added as the iterations advance towards the final solution (each new conjugate vector is calculated based on the previous ones).

The CGM was applied to contact problems by Polonsky and Keer (Polonsky and Keer, 1999) to solve numerically non-adhesive (Hertz) contacts on a HS. It has been also adapted to adhesive contacts on HS by Bazrafshan et al. (Bazrafshan et al., 2017) and Rey et al. (Rey et al., 2017) The CGM implementation of Bazrafshan et al. (Bazrafshan et al., 2017) will be used in this section to compare numerical results with the analytical solutions of the MD model and in the next section to examine the edge compliance contribution to adhesive contacts near the edge of a QS. The key aspect of the CGM implementation for adhesive contacts, in comparison to the non-adhesive version, is the consideration of the tensile contribution to both contact pressure distribution (Equation 11) and force balance during the iterative optimization.

The BEM involved by the CGM used was performed with a custom programming code in Mathematica 10.3 (Wolfram Research, 2015) (see Disclaimer). The convergence of the numerical solution was defined such that, for a given load, the calculated contact pressure distribution corresponded to a resultant load that differed less than 0.01 nN (absolute error) by the considered load. In Figure 2 are shown few comparisons between BEM calculations and theoretical results for both non-adhesive (Hertz) and adhesive (MD) contacts on a HS. The theoretical surface stress and deformation curves were plotted (refer to the continuous curves in Figure 2) as a function of radial distance from the indentation point (arbitrary considered at $x_{\mathrm{c}} = 100.0\ \mathrm{nm}$). With the increase of the Maugis parameter λ, the tensile stress σ_0 increases and, in the same time, the tensile region nearby the edge of a MD contact reduces. The curves were calculated for a rigid indenter of radius $R = 20.0\ \mathrm{nm}$ on a HS of Young's modulus $E = 10.0\ \mathrm{GPa}$ and Poisson's ratio $\nu = 0.3$ at an applied load of $75.0\ \mathrm{nN}$. The work of adhesion for all the MD contacts was considered $w = 0.1\ \mathrm{J/m^2}$, which, for the involved contact geometries, amounts to tensile stresses outside contacts of $0.1\ \mathrm{GPa}$, $0.4\ \mathrm{GPa}$, $0.8\ \mathrm{GPa}$, $1.1\ \mathrm{GPa}$, and $1.5\ \mathrm{GPa}$ for $\lambda = 0.1$, $\lambda = 0.5$, $\lambda = 1.0$, $\lambda = 1.5$, and $\lambda = 2.0$, respectively.

For Hertz and MD with $\lambda = 0.1$, $\lambda = 0.5$, and $\lambda = 1.0$ contacts, the cell size on each direction was $0.234\ \mathrm{nm}$ (the calculation region, H-surface in Figure 1a, was assumed to be

$30\ \mathrm{nm} \times 30\ \mathrm{nm}$ with $N = 128$ grid nodes along each axis). As can be seen in Figure 2, BEM reproduces the dependences of both compressive and the tensile regions very well for Hertz and MD contacts of $\lambda = 0.1,\ \ \lambda = 0.5$ contacts but small deviations are observed between the theoretical and BEM curves in the tensile region around the edge of the contact for the $\lambda = 1.0$ curves. Such discrepancies would be enhanced further for larger values of λ if the same discretization will be used. To mitigate this, for $\lambda = 1.5$ and $\lambda = 2.0$ MD contacts, the cell size on each direction was decreased to 0.039 nm (meshed surfaces at $20\ \mathrm{nm} \times 20\ \mathrm{nm}$ with $N = 512$ grid nodes along each axis) to provide a finer mesh for the tensile region at the edge of the contact where the stress varies rapidly with the increase in λ. Because of this higher discretization, the BEM curves significantly improve in the tensile region even for larger λ values (refer to the insets of Figures 2b and 2d); for very large values of λ ($\lambda > 5.0$) the modeling becomes impractical (Wu, 2006; Rey et al., 2017). It is also worth pointing out that measurable quantities like contact area, indentation depth, pull-off force, and contact stiffness of MD contacts show no significant variations for λ greater than 1.0 at loads greater than the pull-off force. As such, even a coarser discretization will provide reasonable results for a measurement analysis.

3. Boundary element method for Hertz and Maugis-Dugdale contact mechanics on quarter-space

The problem of an elastic QS with one normally loaded surface and one load-free surface was first addressed by Hetenyi (Hetenyi, 1970) who used the method of overlapping loaded half-spaces. Thus, the QS ($x > 0, -\infty < y < \infty, z > 0$) shown in Figure 1a is replaced in Figure 1b by the intersection of two half-spaces: One horizontal HS ($-\infty < x < \infty, -\infty < y < \infty, z > 0$) (shown in pink in Figure 1b) with the free-surface H and one vertical HS ($x > 0, -\infty < y < \infty, -\infty < z < \infty$) (shown in green in Figure 1b) with the free-surface V. As a result, the load F applied normally at position $(x_\mathrm{c}, 0, 0)$ on the H-surface of the QS (refer to Figure 1a) is replaced in the equivalent problem by equivalent loads symmetrically distributed with respect to the edge of the QS: $F_\mathrm{H}(x_\mathrm{c}, y_\mathrm{c}, 0)$ and $F_\mathrm{H}(-x_\mathrm{c}, y_\mathrm{c}, 0)$ on the H-surface and $F_\mathrm{V}(0, y_\mathrm{c}, z_\mathrm{c})$ and $F_\mathrm{V}(0, y_\mathrm{c}, -z_\mathrm{c})$

on the V-surface (refer to Figure 1b). Due to the involved symmetry, only normal stresses will be generated on the faces of the QS, without shear stresses.

The problem is reduced to find the equivalent pressure distributions, $p_{\mathrm{H}}(x,y)$ on the H-surface and $p_{\mathrm{V}}(y,z)$ on the V-surface, such that the stresses generated by these loads on the H-surface of the QS will match the contact pressure distribution $p(x,y)$ produced by the applied load F on the H-surface while keeping the V-surface of the QS load-free. In the original method, Hetenyi used an iterative process to find approximate values for F_{H} and F_{V} but, recently, Zhang et al. (Zhang et al., 2013) developed a matrix formulation to directly determine the limit values of F_{H} and F_{V} for non-adhesive contacts on QS.

In the matrix notation adopted by Zhang et al. (Zhang et al., 2013), the stresses generated on the V and H faces of the QS by the equivalent loads F_{H} and F_{V} and their symmetrical images are

$$\boldsymbol{\sigma}_{xx}^{\mathrm{H}\to\mathrm{V}} = \mathbf{S}_{p_{\mathrm{H}}(x,y)\to\mathrm{V}} \cdot \boldsymbol{p}_{\mathrm{H}}(x,y) + \mathbf{S}_{p_{\mathrm{H}}(-x,y)\to\mathrm{V}} \cdot \boldsymbol{p}_{\mathrm{H}}(-x,y) = \mathbf{M} \cdot \boldsymbol{p}_{\mathrm{H}}(x,y) \tag{18}$$

and

$$\boldsymbol{\sigma}_{zz}^{\mathrm{V}\to\mathrm{H}} = \mathbf{S}_{p_{\mathrm{V}}(y,z)\to\mathrm{H}} \cdot \boldsymbol{p}_{\mathrm{V}}(y,z) + \mathbf{S}_{p_{\mathrm{V}}(y,-z)\to\mathrm{H}} \cdot \boldsymbol{p}_{\mathrm{V}}(y,-z) = \mathbf{N} \cdot \boldsymbol{p}_{\mathrm{V}}(y,z), \tag{19}$$

where $\mathbf{S}$ are influence coefficient matrices introduced in Equation 14. The contact pressures and stresses can be represented by one-dimensional vectors of length N^2 and the influence coefficient matrices $\mathbf{M}$ and $\mathbf{N}$ as $N^2 \times N^2$ arrays. When the two HS are overlapped, the force balance on the H and V faces of the resulting QS gives

$$-\boldsymbol{p}_{\mathrm{H}} + \boldsymbol{\sigma}_{zz}^{\mathrm{V}\to\mathrm{H}} = -\boldsymbol{p}_{\mathrm{H}} + \mathbf{N} \cdot \boldsymbol{p}_{\mathrm{V}} = -\boldsymbol{p} \tag{20}$$

and

$$-\boldsymbol{p}_{\mathrm{V}} + \boldsymbol{\sigma}_{xx}^{\mathrm{H}\to\mathrm{V}} = -\boldsymbol{p}_{\mathrm{V}} + \mathbf{M} \cdot \boldsymbol{p}_{\mathrm{H}} = 0. \tag{21}$$

By combining the above two equations, the equivalent HS-pressure distributions $\boldsymbol{p}_{\mathrm{H}}$ and $\boldsymbol{p}_{\mathrm{V}}$ are found as functions of the given contact pressure distribution $\boldsymbol{p}$:

$$\boldsymbol{p}_{\mathrm{H}} = (\mathbf{I} - \mathbf{N} \cdot \mathbf{M})^{-1} \cdot \boldsymbol{p} \tag{22}$$

and

$$\boldsymbol{p}_{\mathrm{V}} = \mathbf{M} \cdot \boldsymbol{p}_{\mathrm{H}} = \mathbf{M} \cdot (\mathbf{I} - \mathbf{N} \cdot \mathbf{M})^{-1} \cdot \boldsymbol{p}. \tag{23}$$

Once $\boldsymbol{p}_{\mathrm{H}}$ and $\boldsymbol{p}_{\mathrm{V}}$, are found, they and their images are used to calculate stresses and deformations on any cross-section of the QS. In particular, the deformation produced by $\boldsymbol{p}_{\mathrm{H}}$ and its image on the H-surface

$$\boldsymbol{u}_z^{\mathrm{H}} = \mathbf{U}_{p_{\mathrm{H}}(x,y)\to\mathrm{H}} \cdot \boldsymbol{p}_{\mathrm{H}}(x,y) + \mathbf{U}_{p_{\mathrm{H}}(-x,y)\to\mathrm{H}} \cdot \boldsymbol{p}_{\mathrm{H}}(-x,y), \tag{24}$$

where $\mathbf{U}$ are the influence coefficient matrices defined in Equation 15, will be used in the CGM of the QS problem. Notably, due to symmetry, the contributions from $p_{\mathrm{V}}(y,z)$ and $p_{\mathrm{V}}(y,-z)$ to the deformation of the H-surface of the QS cancel each other. The same is true for the deformations produced by $p_{\mathrm{H}}(x,y)$ and $p_{\mathrm{H}}(-x,y)$ on the V-surface of the QS. In summary, the QS problem is reduced to two HS problems in terms of p_{H} and p_{V}, which are related to the contact pressure distribution p through influence coefficient matrices.

The CGM algorithm developed here for an adhesive contact on QS combines the CGM used by Zhang et al. (Zhang et al., 2013) for the non-adhesive contact on a finite-length line (Zhang et al., 2016) with the CGM used by Bazrafshan et al. (Bazrafshan et al., 2017) for an adhesive contact on HS. The main steps of the new algorithm are as following: 1) for a given load F, set the initial values of the contact pressure distribution p over the H-surface (*e.g.*, constant values over a starting area); 2) calculate the equivalent pressure distribution p_{H} and its image; 3) use DC-FFT to calculate the normal deformation u_z^{H} of the H-surface due to p_{H} and its image; 4) use the CGM iteration for an adhesive MD contact (Bazrafshan et al., 2017) to calculate the contact pressure distribution p over the H-surface; 5) if the load calculated from the updated contact pressure p is within the specified tolerance then proceed to step 6, otherwise go back to step 2; 6) calculate the final equivalent pressure distribution p_{H} and its image; 7) use DC-FFT to calculate the final normal deformation u_z^{H} of the H-surface due to p_{H} and its image.

In the next section, results of the MEB using the CGM implemented in the matrix formulation of the QS geometry will be discussed for Hertz and MD with $\lambda = 0.1,\ \lambda = 0.5$, and $\lambda = 1.0$ MD contacts, respectively. The QS discretization was at 128×128 grid nodes on each of the $30\ \mathrm{nm} \times 30\ \mathrm{nm}$ facet of the QS. The simulated contacts were with a rigid indenter of radius $R = 20.0\ \mathrm{nm}$, on a QS of Young's modulus $E = 10.0\ \mathrm{GPa}$ and Poisson's ratio $\nu = 0.3$, the work of adhesion for all the MD contacts was $w = 0.1\ \mathrm{J/m^2}$, and the applied load was varied up to a maximum value of $75.0\ \mathrm{nN}$. As a validation point, the results of Zhang et al. (Zhang et al., 2013) are reproduced in the Appendix for the case of a non-adhesive contact on a QS under a prescribed Hertzian contact distribution.

4. Results and discussion

Based on the BEM results of the new CGM for adhesive contacts on QS, the analysis of the surface stress and deformation on QS can be performed in detail for any of the considered contact interactions. As an example, in Figure 3a are shown the stress and deformation profiles overlapped over the surfaces of the indenter (rigid) and QS (deformable) for an adhesive contact described by the Maugis parameter $\lambda = 0.5$ under a load of $75.0\ \mathrm{nN}$ at $x_c = 5.0\ \mathrm{nm}$ from the QS edge. The 3D-view of the calculated contact pressure distribution is shown in Figure 3b, with both tensile (positive stress) and compressive (negative stress) regions of the contact. It is noted that at this location (contact point about one contact radius from the edge), the symmetry of the stress distribution is disturbed by the edge proximity, a $0.7\ \mathrm{nm}$ shift being measured along the x axis between the location of the maximum compressive stress and the point of contact.

To assess the effect of the edge on QS contacts, surface stress and deformation cross-sections along the x axis were calculated for contacts at various distances from the QS edge and they are shown in Figure 4 at positions $x_c = 5.0\ \mathrm{nm}$ and $x_c = 20.0\ \mathrm{nm}$ for the same applied load of $75.0\ \mathrm{nN}$. Close to the QS edge, the stress and deformation profiles were observed to deviate significantly from their HS counterparts (with the location of the maximum compressive stress shifted from the position of contact). Such effect of the edge compliance was previously

described by Hanson and Keer (Hanson and Keer, 1990) for non-adhesive contacts near a QS edge but only in terms of stress distribution. As can be seen in Figure 4, for both non-adhesive and adhesive contacts, the edge compliance effect is even more pronounced for deformations than stresses: While at $x_c = 15.0\ \mathrm{nm}$ (not shown in Figure 4) and $x_c = 20.0\ \mathrm{nm}$ there is no visible difference between the HS and QS stress curves, clear differences are observed in their surface deformation dependences. Thus, the edge compliance accounts for 30 % and 8 % increase in the indentation depth at $x_c = 5.0\ \mathrm{nm}$ and $x_c = 20.0\ \mathrm{nm}$, respectively, for both non-adhesive and adhesive contacts. This will be reflected also in the contact stiffness of the contact, a quantity that is commonly determined in indentation-type measurements for elastic property characterizations.

The stress changes due to proximity to QS edge are observed not only in the surface stress curves but also in the subsurface stress distributions. In Figure 5 are shown the differences between the σ_{zz} and σ_{xx} stress contours in the *ZX* plane of the QS for the adhesive MD $\lambda = 0.1$ contact at $x_c = 5.0$ nm from the free edge of the QS and those for the same adhesive contact in the middle of a HS; the contours were calculated based on the influence functions of the Love's solution over the grid patches of the H and V surfaces. As can be seen in Figure 5a, the σ_{zz} contours for the QS contact are similar to those for the HS contact with the exception of two details: 1) The appearance of a tensile zone near to the edge of the QS with reduction in the compressive contact region and 2) The stress disturbance imposed by this tensile stress along the x axis, which also appears as a shift between the maximum stress location and the contact point. This shift is more prominent at the surface and attenuates in the lower stress contours below the surface. The tensile stress zone on the non-edge side of the contact is almost unaffected by the edge presence.

The contours of the σ_{xx} stress in the *ZX* plane of the QS show also few notable differences from their HS counterparts (refer to Figure 5b). Thus, as in the case of σ_{zz} contours, there is a shift towards the inner part of the QS due to the presence of a tensile stress at the edge of the QS. However, unlike the σ_{zz} contours, the disturbance on the σ_{xx} contours is not only in the shift location but also in strength and in the non-edge tensile zone: The compressive σ_{xx} under the

indenter decreases faster with depth in the QS contact than in the HS contact and the non-edge tensile zone extends more and almost double in magnitude for the QS contact. Similar features in the σ_{xx} contours in the *ZX* plane of the QS were also observed for a non-adhesive contact near the edge of the QS (Hanson and Keer, 1990). In comparison with the non-adhesive contacts, these features are further enhanced in an adhesive contact due to the presence of the tensile stress in the annular region around the contact.

It is also worth pointing out that while the edge proximity imposes notable perturbations on the stress distributions along the x axis these perturbations are negligible along the y axis. In Figure 6 are shown the contact regions including the annular outer-contact adhesive regions as a MD $\lambda = 0.1$ contact under a load of 75.0 nN was moved away from the QS edge. In comparison to the contact area of its HS counterpart contact, the QS contact has the same extent along the y axis but shrinks along the x axis to adjust a non-contact adhesive region.

The edge effect manifests also in the deformation fields around the contact (*e.g*. surface deformation plots as a function of position at a given applied force as in Figure 4), which can be measured for example as the indentation depth by indentation-type instruments (instrumented nanoindentation and atomic force microscopes). These dependences can be analyzed in terms of contact position and applied contact force. In Figure 7 are shown few relevant examples, namely how the force dependence of the indentation depth changes for non-adhesive and adhesive (here shown only for the adhesive parameter $\lambda = 0.1$) contacts with respect to the distance from the QS edge. For a given distance from the edge, the indentation depth was calculated as a function of the applied contact force by the BEM described above for an adhesive contact on the QS. For baseline comparison, BEM results for HS were overlapped on the theoretical dependences calculated by the analytical models. For a given applied force, there is an increase in the indentation depth as the contact point approaches the edge due to edge compliance (also inferred from the surface deformation curves shown in Figure 4 for an applied force of 75.0 nN). Moreover, as can be seen in Figure 7, at a given position this increase becomes more pronounce with the increase in the applied force. These behaviors are similar for both non-adhesive and adhesive contacts. For the adhesive contact ($\lambda = 0.1$ in Figure 7), it can be also

deduced a reduction in the adhesive force of the contact at the inflexion point of the force dependence curve of the indentation depth (refer to the range of negative applied force in Figure 7). This is consistent with the reduction in the adhesive annular region of the contact shown in Figure 6. As pointed out in Bazrafsan et al. (Bazrafshan et al., 2017), no further calculations were possible by the CGM beyond the inflexion point of the MD curves due to the existence of two different values of the indentation depth for one applied force.

Once the force dependence of the indentation depth was determined, the contact stiffness was calculated as the force derivative with respect to the indentation depth, $k_c = \partial F/\partial \delta$. Analytical expressions for the contact stiffness of adhesive contacts on HS can be found elsewhere (Pietrement and Troyon, 2000; Stan et al., 2014). For the contacts analyzed in Figure 7, the contact stiffness curves versus the applied force are shown in Figure 8a. Once again, the baselines of the BEM calculations are compared with the theoretical curves for the HS cases, non-adhesive (Hertz) and adhesive (MD $\lambda = 0.1$) over the entire range of applied forces. Like the indentation depth curves, the contact stiffness curves vary with the contact position from the edge of the QS and with the applied force. Thus, for a given applied force, there is a pronounce decrease in the contact stiffness as the contact point moves closer to the edge. This is the so-called edge compliance and Figure 8 details quantitatively its dependence. For a given position, there is also a variation in the edge compliance as a function of force, starting from low applied forces (above zero for non-adhesive contacts and above the pull-off force for adhesive forces) and progressively increasing with the increase in the applied force. The effect of adhesion on the contact stiffness declines at applied forces larger than the adhesion force and the curves merge towards the non-adhesive dependence (Hertz for the HS case). Furthermore, in Figure 8b are shown the relative variations of few QS contact stiffnesses (inverse of the edge compliance) with respect to their HS counterparts as a function of position and applied force. At each selected contact position from the edge, the curves show consistent dependences as a function of the adhesive parameter, going from non-adhesive to adhesive. The most pronounce increase in the edge compliance is shown here by the $\lambda = 0.1$ curves. For a given location, as the applied force increases, the differences between adhesive and non-adhesive curves diminish and they bundle together towards a common dependence for each location. It is worth pointing out that a

significant edge effect is observed even far away from the edge, *e.g.* at $20.0\ \mathrm{nm}$ distance from the edge (about $4a_c$) there is 5 % decrease in the contact stiffness at $75.0\ \mathrm{nN}$. This decrease in the contact stiffness varies almost exponentially with the distance from the point of contact to the QS edge: At $75.0\ \mathrm{nN}$ load, the decrease in contact stiffness is 10 % at $15.0\ \mathrm{nm}$, 15 % at $10.0\ \mathrm{nm}$, and 30 % at $5.0\ \mathrm{nm}$. Such significant increases in the edge compliance, as a function of location and applied force, are relevant in interpreting nanoscale mechanical property measurements by atomic force microscopy for example on samples with edge geometries and large topographical variations.

Conclusions

In this work, the effect of edge compliance on the contact mechanics of rigid spherical indenters in adhesive contact with an elastic QS was investigated as a function of applied load, distance to the edge of the QS, and adhesive coupling. The problem of adhesive contacts on a QS was analyzed in the matrix formulation of the CGM with the adhesive part of the contact interaction modeled as a Maugis-Dugdale adhesive coupling. Due to the considered adhesive interaction, qualitative and quantitative changes were observed in the stress and deformation fields in comparison to their HS counterparts. In contrast to the non-adhesive contacts on QS, enhancements in the tensile regions around contacts in the proximity to the QS edge were noted. The effect of the edge compliance was also detailed in measurable quantities like indentation depth and contact stiffness. For these quantities, separated contributions were rationalized in terms of edge vicinity and adhesive interaction. The developed methodology is intended for the analysis of contact mechanics on a sample with edge geometries to correctly separate the material and geometrical contributions to the measured indentation response of the sample.

Disclaimer

Certain commercial equipment, instruments, or materials are identified in this document. Such identification does not imply recommendation or endorsement by the National Institute of

Standards and Technology, nor does it imply that the products identified are necessarily the best available for the purpose.

Appendix

A validation for the BEM algorithm developed in this work is shown here in comparison to the results of Zhang et al. (Zhang et al., 2013) and Hanson and Keer (Hanson and Keer, 1990) for a non-adhesive contact on the edge of a QS. The QS discretization was at 128×128 grid nodes on each of the $30\ \mathrm{nm} \times 30\ \mathrm{nm}$ facet of the QS. The simulated contacts were with a rigid indenter of radius $R = 20.0\ \mathrm{nm}$, on a QS of Young's modulus $E = 10.0\ \mathrm{GPa}$ and Poisson's ratio $\nu = 0.3$, and at an applied load of $75.0\ \mathrm{nN}$. For these parameters, the HS Hertz contact radius is $a = 4.7\ \mathrm{nm}$ and the contact pressure at the middle of the contact is $p_0 = 1.6\ \mathrm{GPa}$. As in the contact configuration considered by Hanson and Keer (Hanson and Keer, 1990) and Zhang et al. (Zhang et al., 2013), the point of contact was chosen at the edge of QS and the contact pressure distribution $p_0\sqrt{1-(r/a)^2}$ remains Hertzian during contact. As can be seen in Figure A1 for the σ_{zz} and σ_{xx} stress contours in the *ZX* plane of the QS, there is a very good match between the current results and those reported by Zhang et al. (Zhang et al., 2013).

References

1. Hanson, M. T, Keer, L. M., 1991. Analysis of edge effects on rail-wheel contact. Wear. 144, 39-55.
2. Yu, C. C., Keer, L. M., 1996. Edge effect on elastic-plastic rolling/sliding contacts. Computational mechnaics. 18, 259-268.

3. Jakes, J. E., Frihart, C. R., Beecher, J. F., Moon, R. J., Resto, P. J., Melgarejo, Z. H., Surez, O. M., Baumgart, H., Elmustafa, A. A., Stone, D. S., 2009. Nanoindentation near the edge. J. Mater. Res. 24, 1016-1031.
4. Jakes, J. E., Stone, D.S., 2010. The edge effect in nanoindentation. Phil. Mag. 91, 1387–1399.
5. Stan, G., Mays, E., Yoo, H. J., King, S. W., 2016. Nanoscale tomographic reconstruction of the subsurface mechanical properties of low-k high-aspect ratio patterns. Nanotechnology. 27, 485706 (9pp).
6. Stan, G., Gates, R.S., Hu, Q., Kjoller, K., Prater, C., Singh, K. J., Mays, E., King, S. W., 2017. Relationships between chemical structure, mechanical properties and materials processing in nanopatterned organosilicate fins. Beilstein J. Nanotechnol. 8, 863–871.
7. Hetenyi, M., 1970. A general solution for the elastic quarter space. Transactions of the ASME J. Appl. Mech. 37 E, 7076.
8. Love, A. E. H., 1929. The stress produced in a semi-infinite solid by pressure on part of the boundary. Phil. Trans. R. Soc. London. A 228, 377-420.
9. Keer, L.M., Lee, J. C., Mura, T., 1983. Hetenyi's elastic quarter space problem revisited. Int. J. Solids Structures. 19, 497-508.
10. Hanson, M. T., Keer, L. M., 1990. A simplified analysis for an elastic quarter-space. Quart. J. Mech. Appl. Math. 43, 561-588.
11. Keer, L. M., Lee, J. C., Mura, T., 1984. A contact problem for the elastic quarter space. Int. J. Solids Structures. 20, 513-524.
12. Armani, N., Keer, L. M., Mura, T., 1983. Non-Hertzian contact stress analysis for an elastic half-space-normal and sliding contact. Int. J. Solids Structures. 19, 357-373.
13. Zhang, Z. M., Wang, W., Wong, P. L., 2013. An explicit solution for the elastic quarter-space problem in matrix formulation. Int. J. Solids Structures. 50, 976.
14. Zhang, H., Wang, W., Zhang, S., Zhao, Z., (2016). Modeling of finite-length line contact problem with consideration of two free-end surfaces. J. Tribology. 138, 021402-10.
15. Hertz, H., 1881. Ueber die Berührung fester elastischer Körper. J. Reine Angew. Math. 92, 156-171.

16. Huber, M. T., 1904. Zur Theorie der Beruhrung fester elastischer Korper. Ann. Phys. 319, 153–163.
17. Johnson, K. L, 1985. Contact mechanics. Cambridge University Press, Cambridge.
18. Hills, D. A., Nowell., D., Sackfield. A., 1993. Mechanics of elastic contacts. Butterworth-Heinemann Ltd., Oxford.
19. Derjaguin, B. V., Muller, V. M., Toporov, Y. P., 1975. Effect of contact on the adhesion of particles. J. Colloid Interface Sci. 53, 314-326.
20. Johnson, K. L., Kendall, K., Roberts, A. D., 1971. Surface energy and the contact of elastic solids. Proc. Roy. Soc. London. A 324, 301-313.
21. Maugis, D., 1992. Adhesion of spheres: The JKR-DMT transition using the Dugdale model. J. Colloid Interface Sci. 150, 243-269.
22. Bazrafshan, M., de Rooij, M. B., Valefi, M., Schipper, D. J., 2017. Numerical method for the adhesive normal contact analysis based on a Dugdale approximation. Tribology International 112, 117-128.
23. Rey, V., Anciaux, G., Molinari, J. F., 2017. Normal adhesive contact on rough surfaces: efficient algorithm for FFT-based BEM resolution. Comput. Mech. 60, 69-81.
24. Jin, X., Niu, F., Zhang, X., Zhou, Q., Lyu, D., Keer, L. M., Hu, Y., 2016. Love's rectangular contact problem revisited: A complete solution. Tribology International 103, 331-342.
25. Liu, S., Wang, Q., Liu, G., 2000. A versatile method of discrete convolution and FFT (DC-FFT) for contact analyses. Wear. 243, 101-11.
26. Shewchuk, J. R., 1994. An introduction to the conjugate gradient method without agonizing pain. Technical Report No. CMU-CS-94-125, School of Computer Science, Carnegie Mellon University, Pittsburgh, Pennsylvania, March 1994.
27. Polonsky, I. A., Keer, L. M., 1999. A numerical method for solving rough contact problems based on the multi-level multi-summation and conjugate gradient techniques. Wear. 231, 206-219.
28. Wolfram Research, Inc., Mathematica, Version 10.3, Champaign, IL, 2015. http://www.wolfram.com.

29. Wu, J. J., 2006. Numerical analyses on elliptical adhesive contact. J. Phys. D: Appl. Phys. 39, 1899-1907.
30. Pietrement, O., Troyon, M, 2000. General equations describing elastic indentation depth and normal contact stiffness versus load. Journal of Colloid and Interface Science. 226, 166–171.
31. Stan, G., Solares, S. D., Pittenger, B., Erina, N., Su, C., 2014. Nanoscale mechanics by tomographic contact resonance atomic force microscopy. Nano scale. 6, 962.

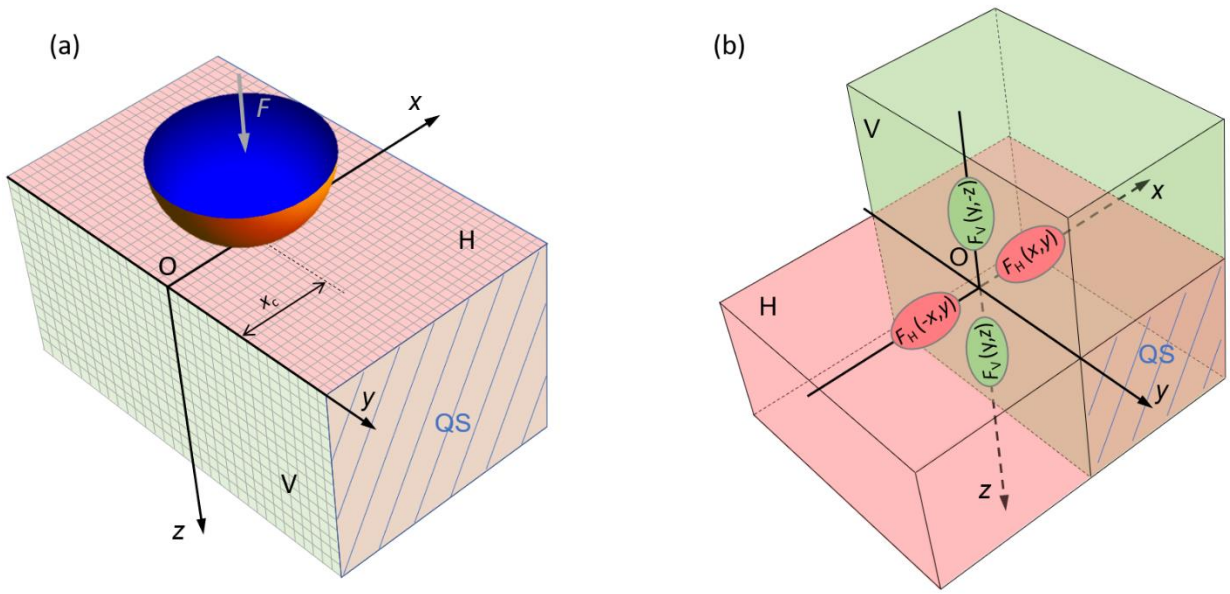

Figure 1. a) Spherical tip indenting the top face *XY* of either a HS or a QS at position $(x_c, 0, 0)$ from the edge. The loaded *XY* face is referred as the H-surface and the load-free *YZ* face of the QS as the V-surface. For the HS case, only the H-surface is considered whereas for the QS case both H-surface and V-surface are included. b) The QS is defined by the intersection of two half-spaces, shown in green and pink colors, respectively. The top surfaces H and V of these two half-spaces are used in the QS calculation. The applied load on the top surface of the QS shown in a) is replaced in b) by equivalent loads, symmetrically distributed around the edge of the QS. *i.e.* the *y* axis. Note that the H and V surfaces are shown in a) as the actual top and left surfaces of the QS whereas in b) they are extended above and to the left of the QS as part of the two equivalent half-spaces. In both a) and b), the front *ZX* cross-section of the actual QS is indicated by a diagonal-stripe pattern.

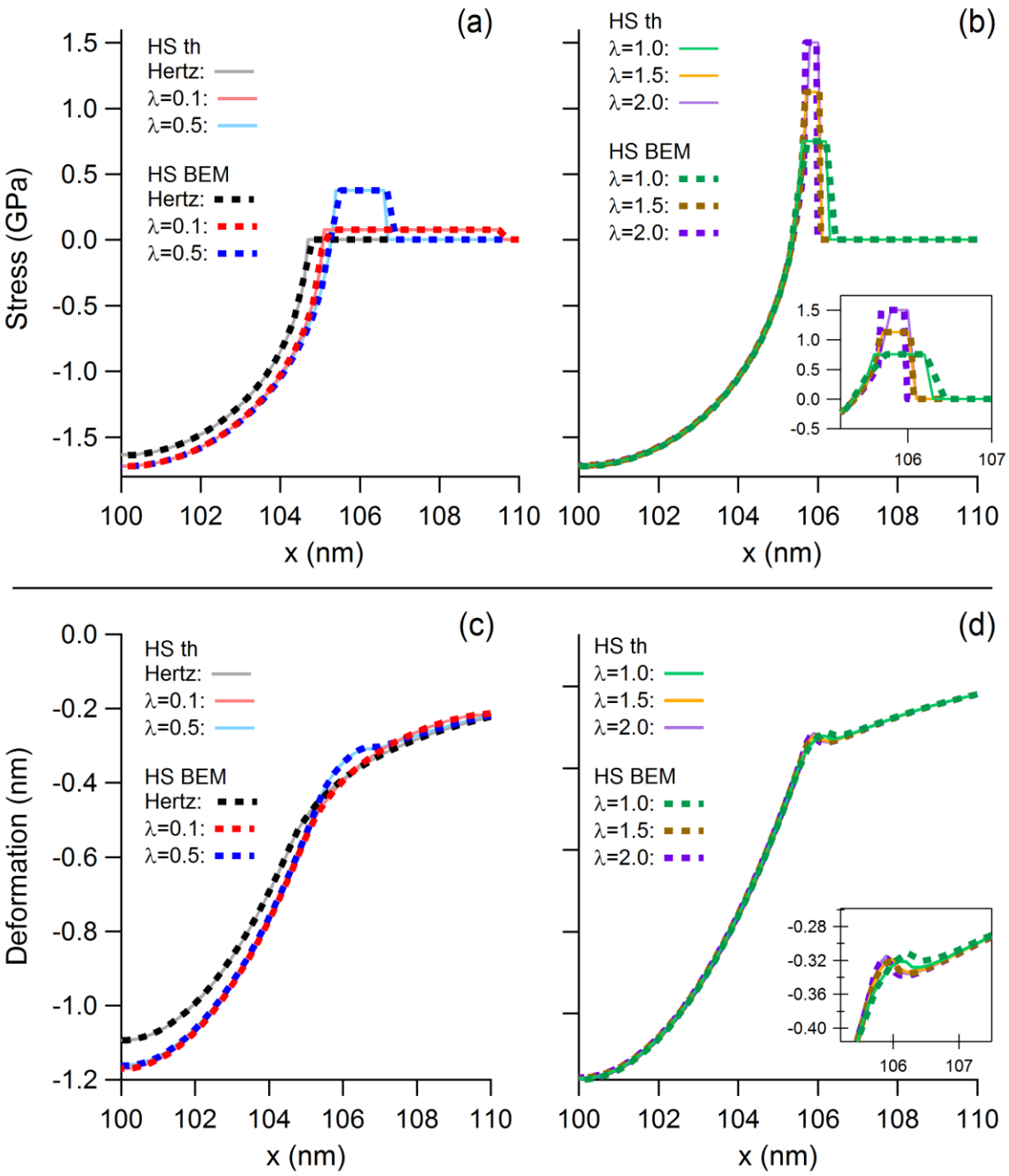

Figure 2. Comparison between surface stress (a) and (b) and deformation (c) and (d) profiles calculated by HS analytical Hertz and MD models (continuous lines) and BEM (dashed lines) with contact position in the middle of HS (see text for details). In all cases the applied load was $F = 75.0$ nN. The insets in (b) and (d) show expended views of the tensile regions of the investigated contacts.

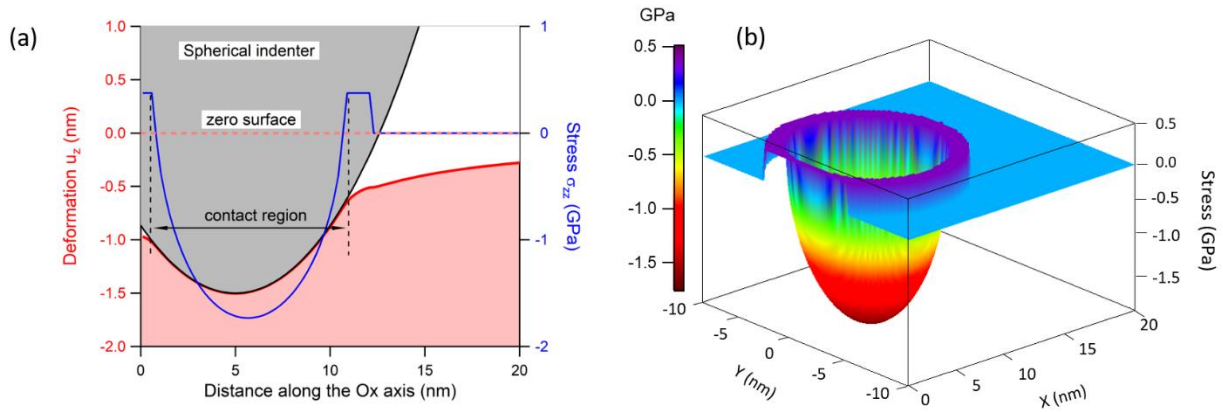

Figure 3. Surface stress and deformation BEM calculations for a spherical indenter ($R = 20.0$ nm) indenting a QS at $x_c = 5.0$ nm from its edge under a load of load of 75.0 nN; the adhesive contact interaction is described by the Maugis parameter $\lambda = 0.5$. a) Cross-section view of the surface deformation (red curve, left axis) and normal surface stress (blue curve, right axis) as overlapped over the tip-sample contact. The zero-surface line denotes the undeformed H-surface of the QS. b) Three-dimensional view of the surface stress distinctively showing the annular region of tensile stress around the contact.

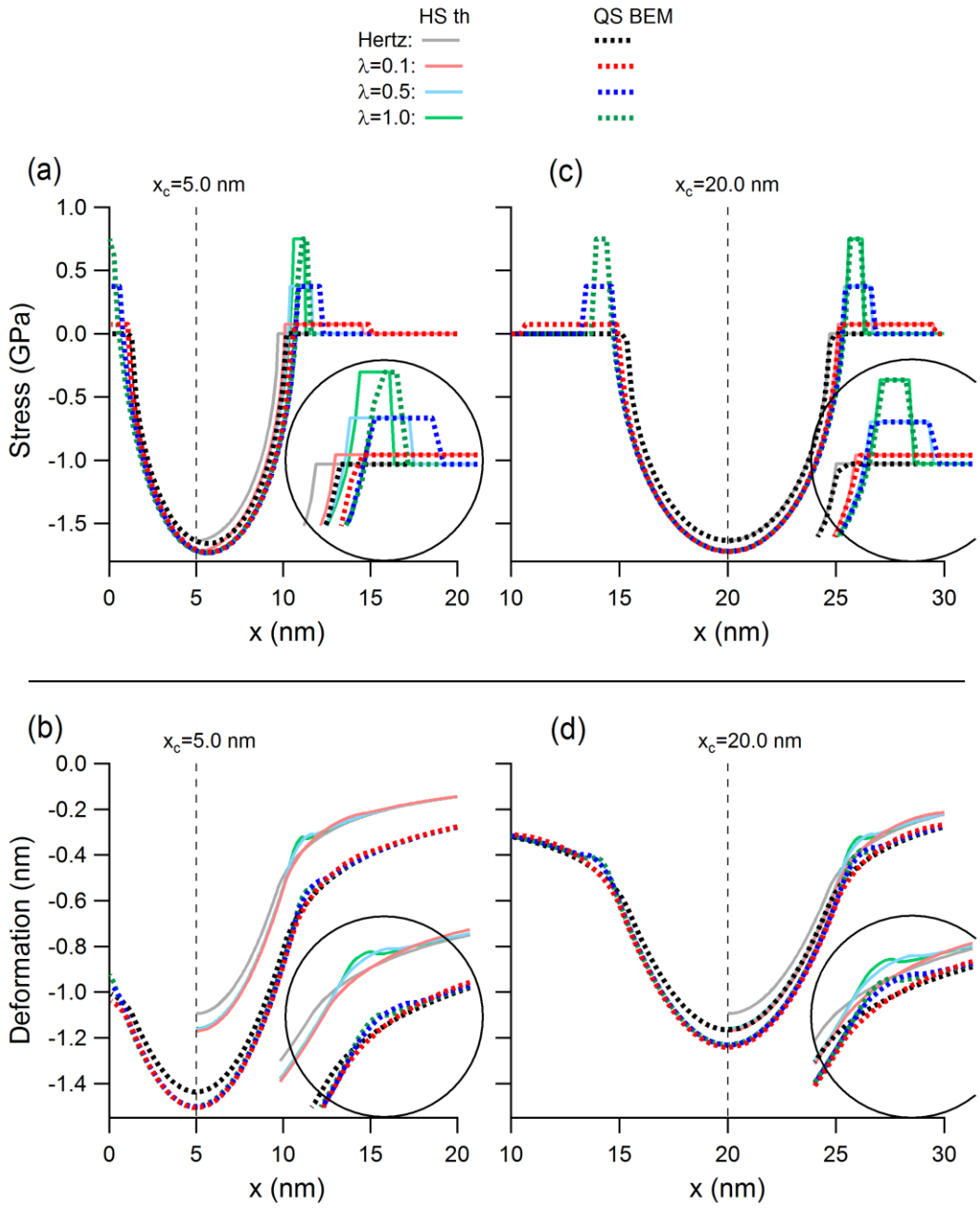

Figure 4. a) and c) Surface stress and b) and d) deformation profiles along the x axis with the contact point at $x_c = 5.0$ nm (a) and b)) and $x_c = 20.0$ nm (c) and d)) from the edge of the QS under an applied load of 75.0 nN. The dashed lines are BEM calculations and the continuous lines are obtained from analytical HS models with the origin shifted at the contact points; the analytical calculations are shown only for half of the contact. The regions around the contact edge are enlarged in the oval insets of the plots. All the plots share the same color code.

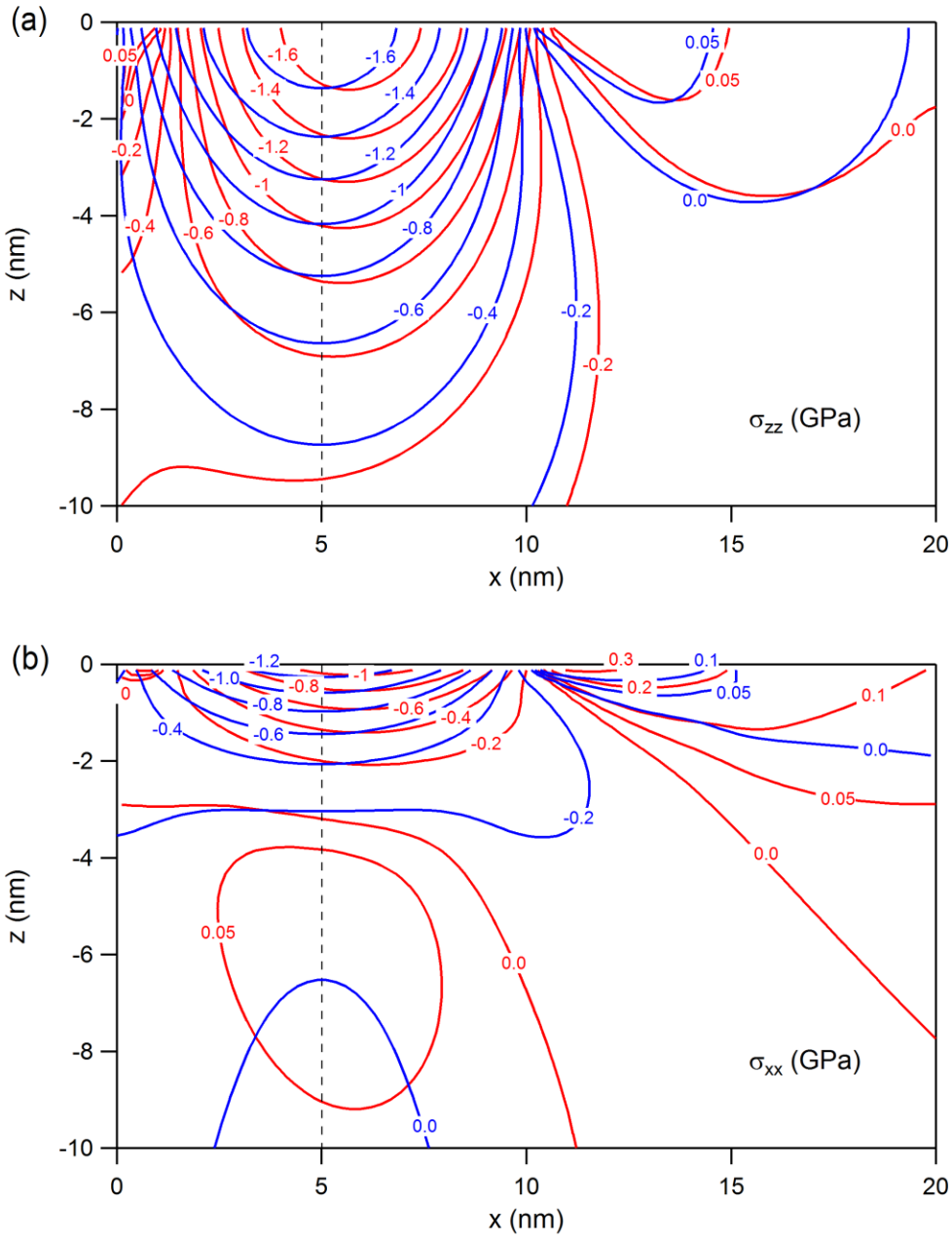

Figure 5. Stresses a) σ_{zz} and b) σ_{xx} in the *ZX* plane of the QS for an adhesive MD $\lambda = 0.1$ contact with the indenter at $x_c = 5.0$ nm from the free edge of the QS (red contours) and in the middle of the HS (blue contours) but shifted at $x_c = 5.0$ nm, respectively. The indentation was performed under a load of 75.0 nN.

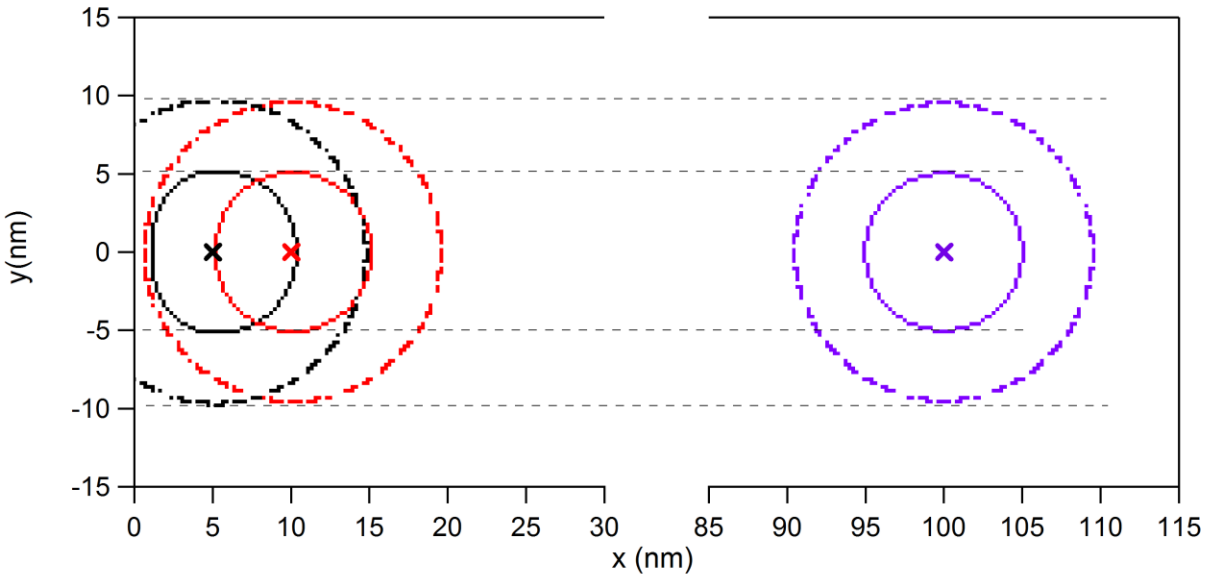

Figure 6. Circumferences of the contact area (continuous line) and annular region (dashed line) at various positions in the *XY* plane for the same applied load of $75.0\ \mathrm{nN}$ and Maugis parameter $\lambda = 0.1$. The dotted horizontal lines show that the projections of these circumferences on the y axis remain unchanged as the center position x_c moves along the x axis (the edge of the QS is at $x = 0.0\ \mathrm{nm}$). The center positions of the indents are marked by solid crosses of the same color as their corresponding circumferences.

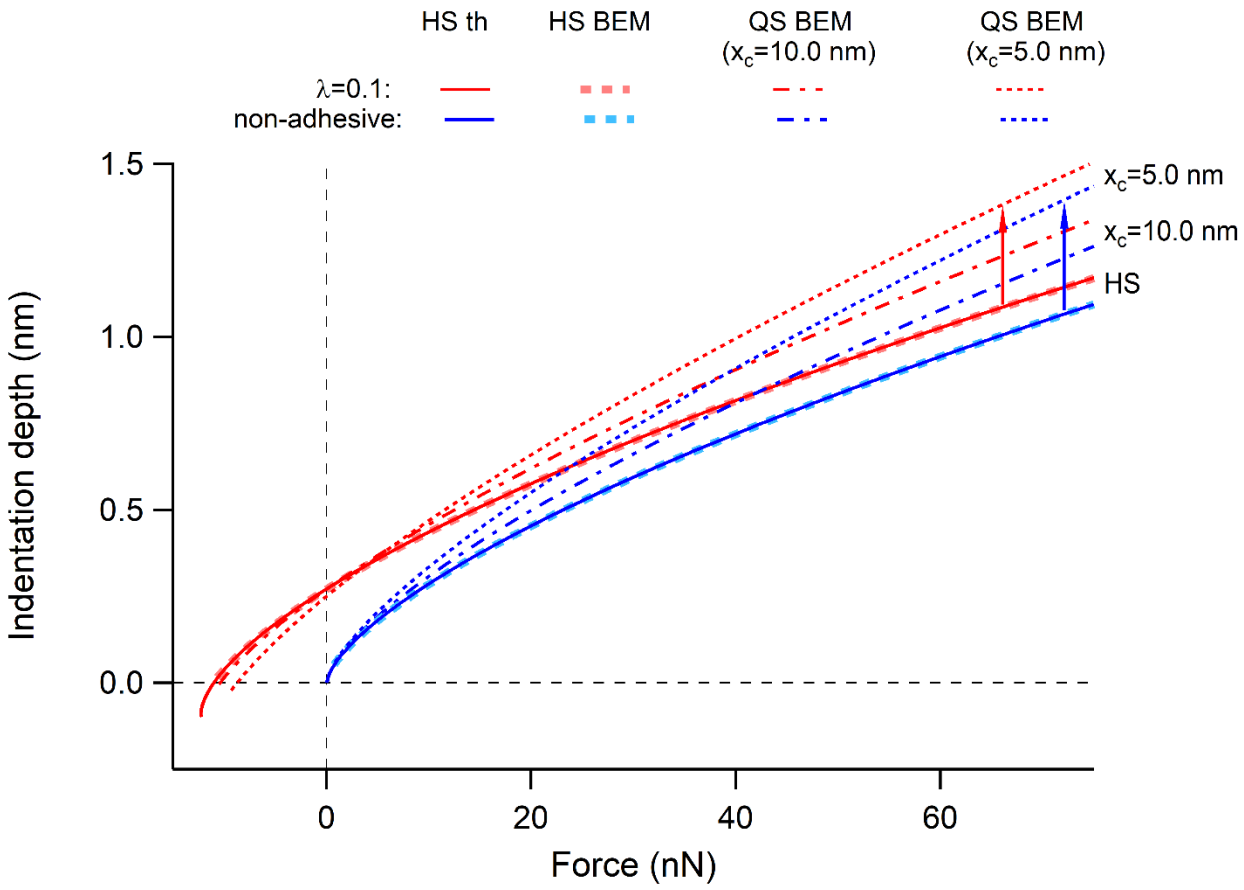

Figure 7. Indentation depth versus applied force curves for different adhesive couplings (non-adhesive and MD $\lambda = 0.1$) as calculated by analytical models and BEM for contact positions at $x_c = 5.0\,\mathrm{nm}$ and $x_c = 10.0\,\mathrm{nm}$ from the edge of the QS. The arrows indicate the differences between the HS contacts and their QS counterparts.

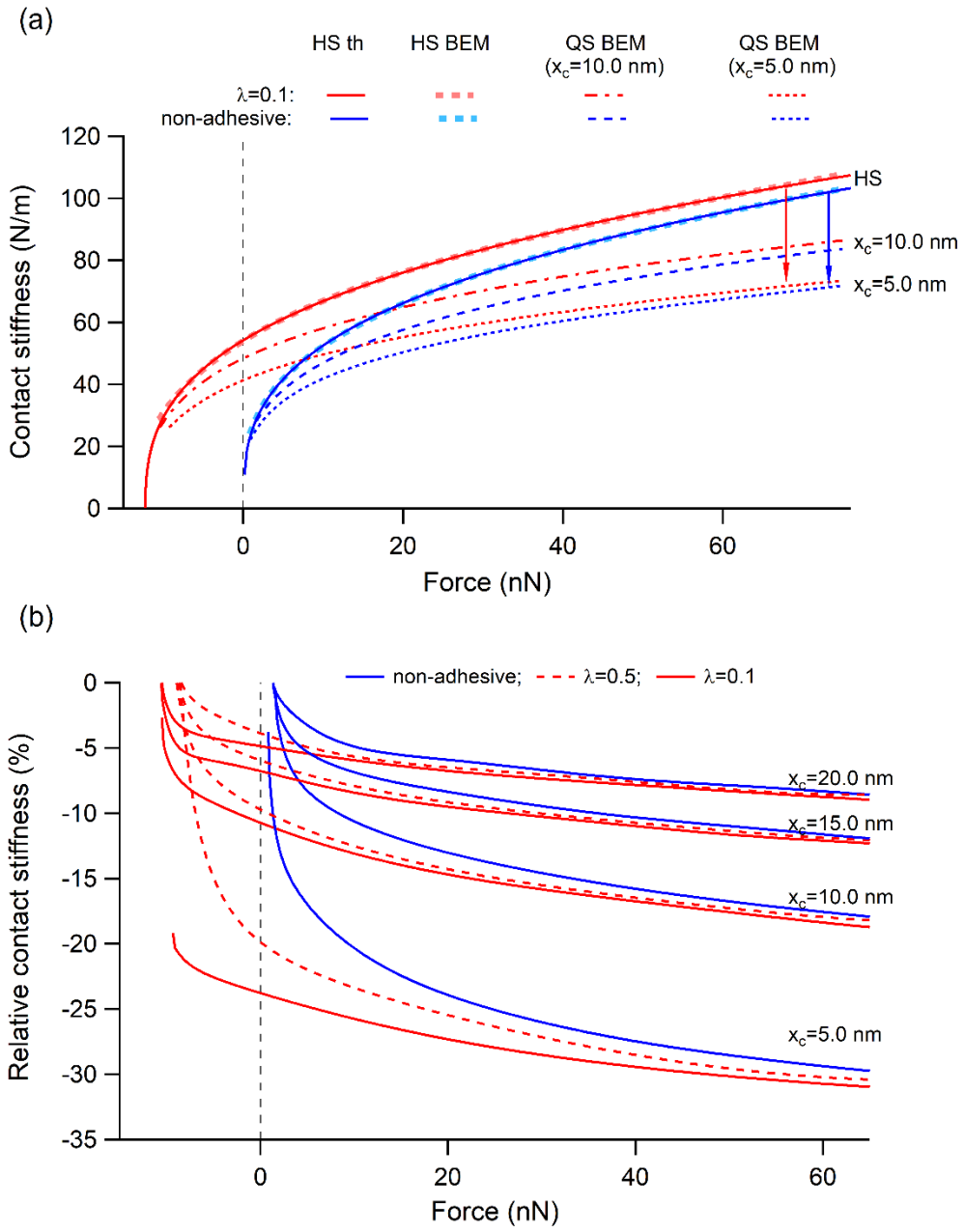

Figure 8. a) Contact stiffness versus applied force curves for different adhesive couplings (non-adhesive and MD $\lambda = 0.1$) as calculated by analytical models and BEM for contact positions $x_c = 5.0\ \mathrm{nm}$ and $x_c = 10.0\ \mathrm{nm}$ from the edge of the QS. The arrows indicate the shifts of the Hertz and MD $\lambda = 0.1$ curves from their HS cases to their $x_c = 5.0\ \mathrm{nm}$ QS counterparts. B) At various locations from the edge of the QS, relative deviations of the contact stiffness values were calculated with respect to their HS counterparts by considering different adhesive couplings (non-adhesive and MD with $\lambda = 0.1$ and $\lambda = 0.5$).

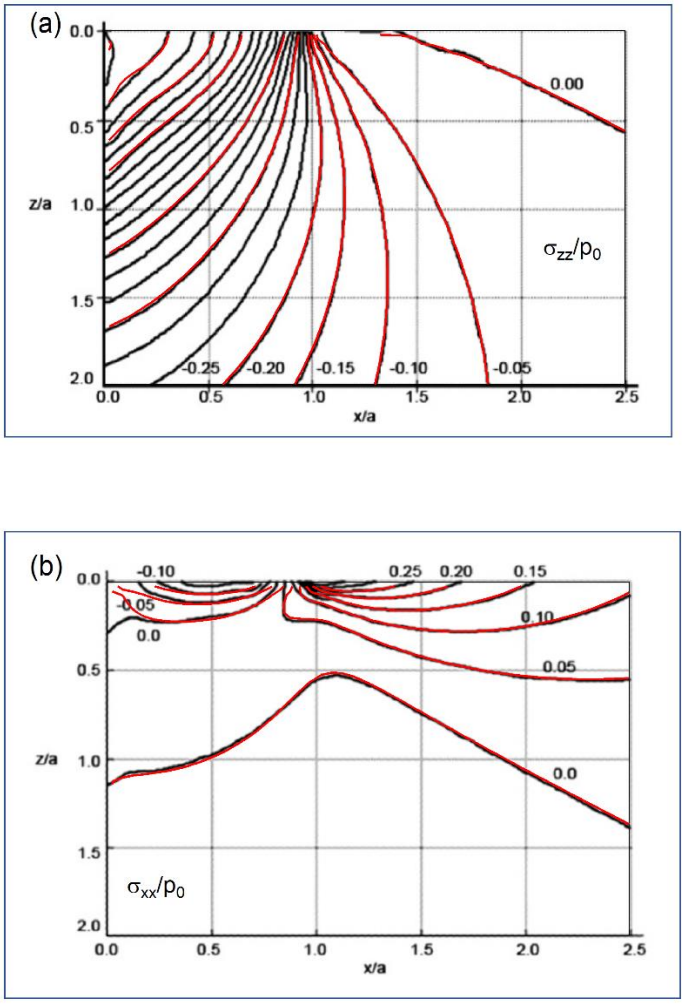

Figure A1. Comparison between the results of the current BEM algorithm (red curves) and those of Zhang et al. (Zhang et al., 2013) (black curves) for the σ_{zz} and σ_{xx} stress contours in the *ZX* plane of the QS. The contact was considered at the edge of the QS with a prescribed Hertz contact distribution. The stress values were normalized to the peak value of the Hertz contact pressure and the coordinates to the Hertz contact radius.